

## RESEARCH ARTICLE

10.1002/2016JD025948

## Key Points:

- The 2014 deployment of the ATTREX mission yielded an extensive data set of TTL cirrus IWC and microphysical properties
- The effective diameter for TTL cirrus exhibited a weak temperature dependence above 192 K but decreased strongly between 192 and 186 K
- New parameterization of the IWC-extinction relationship will improve lidar-derived IWC for climatologically important TTL cirrus clouds

## Correspondence to:

T. D. Thornberry,  
troy.thornberry@noaa.gov

## Citation:

Thornberry, T. D., A. W. Rollins, M. A. Avery, S. Woods, R. P. Lawson, T. V. Bui, and R.-S. Gao (2017), Ice water content-extinction relationships and effective diameter for TTL cirrus derived from in situ measurements during ATTREX 2014, *J. Geophys. Res. Atmos.*, 122, 4494–4507, doi:10.1002/2016JD025948.

Received 16 SEP 2016

Accepted 28 MAR 2017

Accepted article online 29 MAR 2017

Published online 25 APR 2017

## Ice water content-extinction relationships and effective diameter for TTL cirrus derived from in situ measurements during ATTREX 2014

Troy D. Thornberry<sup>1,2</sup> , Andrew W. Rollins<sup>1,2</sup> , Melody A. Avery<sup>3</sup>, Sarah Woods<sup>4</sup> , R. Paul Lawson<sup>4</sup> , Thaopaul V. Bui<sup>5</sup> , and Ru-Shan Gao<sup>1</sup> 

<sup>1</sup>Chemical Sciences Division, NOAA Earth System Research Laboratory, Boulder, Colorado, USA, <sup>2</sup>Cooperative Institute for Research in Environmental Sciences, University of Colorado Boulder, Boulder, Colorado, USA, <sup>3</sup>Atmospheric Composition Branch, NASA Langley Research Center, Hampton, Virginia, USA, <sup>4</sup>SPEC, Inc., Boulder, Colorado, USA, <sup>5</sup>Atmospheric Science Branch, NASA Ames Research Center, Moffett Field, California, USA

**Abstract** The NASA Airborne Tropical Tropopause Experiment (ATTREX) deployment in January–March 2014 yielded more than 34 h of cirrus cloud sampling in the tropical tropopause layer (TTL) over the western Pacific. Cirrus were encountered throughout the TTL, at temperatures between 185 and 207 K, with ice water content (IWC) ranging from  $>10 \text{ mg m}^{-3}$  to below the instrumental detection limit of  $1 \text{ } \mu\text{g m}^{-3}$ . Geometric optical extinction ( $\sigma$ ) values determined from cloud particle probe measurements ranged from  $10^{-3} \text{ m}^{-1}$  to  $<10^{-7} \text{ m}^{-1}$ . The median effective diameter ( $D_{\text{eff}}$ ) for cirrus sampled at  $T > 192 \text{ K}$  was 40–50  $\mu\text{m}$  and exhibited a weak temperature dependence, while colder than 192 K,  $D_{\text{eff}}$  decreased more strongly with decreasing  $T$ . From the ATTREX data, a new parameterization of the IWC- $\sigma$  relationship for TTL cirrus is derived that will improve the estimation of IWC from lidar and optical probe observations of these clouds.

**Plain Language Summary** Cold, high-altitude tropical cirrus clouds are an important component of the climate system but are significantly underconstrained in climate models. Lidar measurements, especially from satellites, have the spatial and temporal coverage to produce statistically meaningful observations for model comparison and validation but do not directly measure quantities such as cloud ice water content that are important predicted quantities in the models. We have used an extensive data set of cloud ice water content and microphysical properties collected during a 2014 aircraft campaign in the western Pacific to derive a new parameterization that will improve the estimation of ice water content from lidar remote sensing measurements of tropical cirrus. With this parameterization, lidar observations can be used to derive a more accurate ice water content for tropical cirrus, in order to improve its treatment in models.

### 1. Introduction

Cirrus clouds cover up to a third of the globe at any time and occur with high frequency in the tropical tropopause layer (TTL), particularly over the western Pacific [Sassen *et al.*, 2008; Massie *et al.*, 2010; Winker *et al.*, 2010]. Cirrus play a significant role in the radiative balance of the TTL [Yang *et al.*, 2010] and produce dehydration of air as it is transported into the stratosphere [e.g., Jensen and Pfister, 2004; Fueglistaler *et al.*, 2009; Randel and Jensen, 2013]. Cirrus in the TTL can result from detrainment of convectively lofted ice or form in situ due to slow vertical advection or wave-driven cooling. TTL cirrus typically have low ice water content (IWC) relative to midlatitude cirrus [Luebke *et al.*, 2013] due to the lower available water content of the air at cold TTL temperatures and are frequently optically thin, resulting in a net radiative heating due to greater longwave absorption than shortwave scattering [Yang *et al.*, 2010].

IWC and cloud effective diameter,  $D_{\text{eff}}$ , are important quantities that relate bulk cloud properties to radiative properties and are prognostic variables in global climate models. Measurements of these quantities are critical for improving the representation of cirrus in the models [Waliser *et al.*, 2009; Baran, 2012; Li *et al.*, 2012]. How cirrus cloud frequency, spatial distribution, and radiative effect will change as the climate changes remain open questions [Zhou *et al.*, 2014; Bretherton, 2015], leading to significant uncertainty in their role as a climate feedback.

Ground-based, airborne, and spaceborne lidars are important tools for studying cirrus clouds but do not directly measure a number of radiatively important cloud properties such as IWC. The Cloud-Aerosol Lidar

with Orthogonal Polarization (CALIOP) instrument on the Cloud-Aerosol Lidar and Infrared Pathfinder Satellite Observations (CALIPSO) satellite produces globally distributed profiles of volume optical extinction ( $\sigma$ ) retrieved from backscatter observations [Young and Vaughan, 2009] with a vertical resolution of 60 m in the TTL. CALIOP is capable of detecting clouds with layer-integrated backscatter as small as  $0.001 \text{ sr}^{-1}$ , corresponding to an estimated minimum  $\sigma$  on the order of  $2 \times 10^{-7} \text{ m}^{-1}$  [Winker et al., 2007; Sassen et al., 2008; Winker et al., 2010; Avery et al., 2012]. Combined radar/lidar measurements can be used to derive cloud IWC for sufficiently dense clouds [Donovan and van Lammeren, 2001; Wang and Sassen, 2002; van Zadelhoff et al., 2007]. However, TTL cirrus frequency and extent is dominated by optically thin clouds [Winker et al., 2010; Yang et al., 2010], which, while visible to lidar, are frequently too optically thin, or contain particles too small, to be detected by radar [Comstock et al., 2002; Heymsfield et al., 2005; Winker et al., 2010; Avery et al., 2012; Heymsfield et al., 2014]. For these thin clouds, empirically derived relationships from in situ measurements are needed to allow calculation of IWC from the lidar-retrieved optical extinction [Heymsfield et al., 2005; Avery et al., 2012; Heymsfield et al., 2014]. Due to the high altitude of TTL cirrus, relatively few in situ measurements of IWC and cloud microphysical properties have been made from which to derive this relationship at the cold TTL temperatures, compared to midlatitude cirrus for which aircraft data are much more abundant [e.g., Luebke et al., 2013; Heymsfield et al., 2014; Krämer et al., 2016]. Extrapolation of results from analysis of midlatitude cirrus to the TTL may not be appropriate, since cirrus formation conditions and mechanisms are different in the TTL [Jensen et al., 2010; Luebke et al., 2013; Randel and Jensen, 2013].

In the present analysis, we use the extensive set of in situ measurements of IWC and cloud microphysical properties acquired during the 2014 deployment of the Airborne Tropical Tropopause Experiment (ATTREX) mission to investigate the relationship between IWC and  $\sigma$  in cold TTL cirrus. The observations are used to develop an IWC ( $\sigma$ ) parameterization that can be used to improve the IWC determination from lidar and optical cloud probe observations of TTL cirrus.

## 2. Measurements

The 2014 deployment of the ATTREX mission from Guam during boreal winter (January–March) yielded more than 34 h of TTL cirrus sampling during eight research flights of the NASA Global Hawk [Jensen et al., 2016]. In the following analysis, we use a definition of TTL cirrus to include clouds found at latitudes between  $20^\circ\text{N}$  and  $12^\circ\text{S}$  (the southernmost latitude reached during ATTREX 2014) and pressure  $< 150 \text{ hPa}$  [Fueglistaler et al., 2009], corresponding to GPS altitudes  $> 14.3 \text{ km}$ . Figure 1 shows the ATTREX 2014 flight tracks and the locations where clouds were encountered, covering a broad region of the TTL over the western tropical Pacific.

### 2.1. Ice Water Content Measurement

Bulk IWC of cirrus clouds was determined using the two-channel, tunable diode laser-based NOAA Water instrument [Thornberry et al., 2015]. The two channels of the instrument are used to make simultaneous measurements of water vapor (WV) through a side-facing inlet and enhanced total water (eTW, water vapor plus inertially enhanced condensed-phase water) through a heated, forward facing inlet. IWC is calculated by subtracting the measured water vapor from the enhanced total water and then dividing by the ice particle enhancement factor (EF) that arises from subsokinetic sampling:

$$\text{IWC} = (\text{eTW} - \text{WV})/\text{EF} \quad (1)$$

The particle size-dependent inertial enhancement is calculated using the parameterization of Eddy et al. [2006] and depends on ambient pressure and temperature and the aircraft true air speed. For particles with diameter greater than  $8 \mu\text{m}$ , the EF is constant and equivalent to the ratio of the geometric volume swept by the inlet to the volumetric sample flow. At typical Global Hawk airspeeds between  $150$  and  $170 \text{ m s}^{-1}$ , the geometric sample volume for cloud particles is approximately  $2.6 \text{ L s}^{-1}$ , and the EF ranged from 33 to 48, depending primarily on altitude. Particles smaller than  $8 \mu\text{m}$  experience a decreasing EF with decreasing diameter, but these particles typically contributed only a small amount to the total cloud IWC. Based on the cloud particle size data for the TTL cirrus encountered during ATTREX 2014, applying the size-independent (large particle) EF for all clouds sampled leads to an IWC error  $< 2\%$  for 98% of observations.

The 1 s detection limit for IWC is typically  $2\text{--}3 \mu\text{g m}^{-3}$  depending on the EF, and the overall uncertainty in the IWC measurement, dominated by systematic uncertainties related to the sampling, is estimated to be  $\sim 20\%$  [Thornberry et al., 2015]. When the total water and water vapor data are averaged over 15 s, the IWC detection

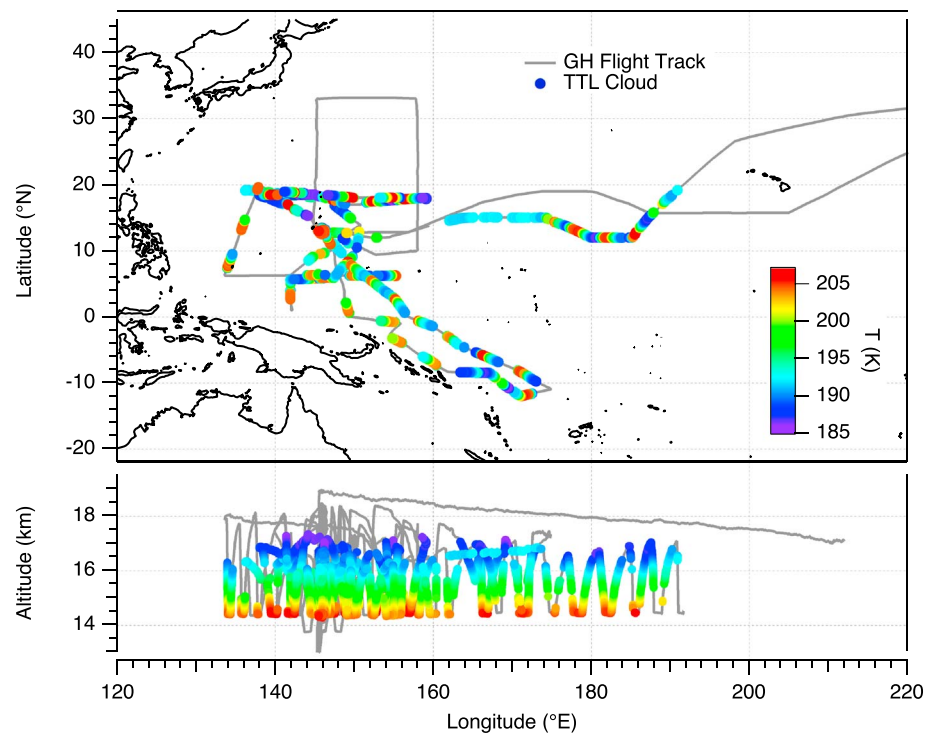


**Figure 1.** (top) Map showing the flight tracks (grey) of the Global Hawk during the ATTREX 2014 deployment from Guam. Symbols along the flight track indicate where cirrus clouds were encountered in the TTL, colored by temperature. (bottom) Vertical profiles of the flight tracks showing the altitudes of the encountered clouds.

limit is improved to  $\sim 1 \mu\text{g m}^{-3}$ , while the overall uncertainty is unchanged. This detection limit is one to two orders of magnitude lower than the direct IWC measurements used in prior analyses [Heymsfield *et al.*, 2005; Davis *et al.*, 2007; Heymsfield *et al.*, 2014] and thus allows the IWC- $\sigma$  relationship to be observed for thinner clouds than previously possible.

## 2.2. Cloud Particle Measurements

Cirrus particle measurements during ATTREX 2014 were made using a wing-mounted SPEC, Inc., Hawkeye combination probe and a standalone Fast Cloud Droplet Probe (FCDP) [O'Connor *et al.*, 2008; Lance *et al.*, 2010] mounted beneath the fuselage. The Hawkeye probe includes a Manufacturer (SPEC, Inc.) instrument designation is "2D-Stereo" and "2D-S" detector optical array probe 2D-S [Lawson *et al.*, 2006] and a FCDP, as well as a Cloud Particle Imager (CPI). During ATTREX the Hawkeye-CPI was operated in triggered mode, allowing the CPI to provide high-resolution imagery for habit identification, while the 2-D-S channels provide quantitative information on the particle size distributions.

FCDPs measure forward scattered light from individual cloud particles to determine the particle diameter in the range from  $1 \mu\text{m}$  to  $50 \mu\text{m}$ . They are designed and calibrated primarily for sizing liquid droplets, and the asphericity and surface roughness of ice particles induces additional uncertainty in the particle size determination. The 2-D-S detector uses photodiode arrays to measure the dimensions and projected area of individual cloud particles with diameters from  $5 \mu\text{m}$  to  $4 \text{mm}$ . For the present analysis, data from the FCDPs and 2-D-S were combined to produce particle size distributions (PSD) using 12 size bins from 1 to  $24 \mu\text{m}$  from the FCDPs, and 40 size bins from 25 to  $855 \mu\text{m}$  from the 2-D-S. The particle concentration in the  $21\text{--}24 \mu\text{m}$  size bin of the FCDP was scaled up by  $4/3$  to account for the gap between that bin and the  $25\text{--}35 \mu\text{m}$  size bin of the 2-D-S. No cloud particles larger than  $855 \mu\text{m}$  were detected by the 2-D-S in the TTL during ATTREX 2014, and less than 3% of the time were particles with diameters larger than  $200 \mu\text{m}$  observed, predominantly at the lowest sampling altitudes ( $< 14.5 \text{ km}$ ) and correspondingly warmest temperatures.

The use of  $25 \mu\text{m}$  as the size at which to merge the 2-D-S and FCDP distributions was determined by instrumental factors. The 2-D-S has a much larger sample volume than the FCDP, producing better statistics in sparse clouds, as well as better measures of particle size and area due to the imaging nature of the

detector. However, the 10  $\mu\text{m}$  resolution of the 2-D-S diode array leads to increased uncertainty in measurements in the smallest size bins. Part of this uncertainty arises because small particles have a very narrow depth of field, reducing the effective sample volume for correct measurement. Out of focus particles may produce broken diffraction patterns, leading to overcounting in smaller size bins. Small particles may fail to occult their full size across the diode array, which leads to undercounting in the correct bin and overcounting in smaller bins. This effect is particularly notable when the mode diameter of the size distribution falls below 20  $\mu\text{m}$ , as occurred at the coldest temperatures during ATTREX. Due to these effects in the smallest 2-D-S bins, FCDP data are used for particles in the size range below 25  $\mu\text{m}$ .

In a number of previous studies investigating cirrus cloud microphysics using aircraft data, artifacts in the measurement of small ice crystal number using instruments similar to the FCDP and 2-D-S were caused by shattering of large ice crystals on the cloud probe tips [e.g., Gayet et al., 1996; McFarquhar et al., 2007; Heymsfield et al., 2006; Heymsfield, 2007; Jensen et al., 2009]. Both the standalone FCDP and Hawkeye probes flown during ATTREX were equipped with tips designed to minimize the potential for large ice particle shatter, and interarrival time analysis was used to further discriminate against any shattering artifacts that might occur. These measures have been shown to be effective in reducing, although not eliminating, the artifacts associated with shattering [Lawson, 2011; Korolev et al., 2013; Korolev and Field, 2015]. Due to the low incidence of large ice particles in the TTL during ATTREX, shattering is not expected to have significantly affected the small sizes of the cloud particle measurements. This conclusion is supported by the lack of any evidence of particle shattering in TTL cirrus in either the 2-D-S data or CPI images.

The sample volume of the standalone FCDP was 0.08  $\text{L s}^{-1}$ , which results in discretization of the reported ice number concentration (INC) in steps of  $\sim 12 \text{ L}^{-1} \text{ bin}^{-1}$ . The sample volume of the Hawkeye FCDP was 0.045  $\text{L s}^{-1}$ , producing even larger steps. Due to the frequently low INC of the sampled TTL cirrus (median value  $\sim 18 \text{ L}^{-1}$ ), this produces sharp discontinuities in the 1 s particle size, mass, and extinction distributions. To ameliorate these discontinuities, the data used in this analysis have been averaged into 15 s periods to produce a standalone FCDP sample volume  $> 1 \text{ L}$ , resulting in a discretization in the data of  $< 1 \text{ L}^{-1} \text{ bin}^{-1}$ . This averaging results in a typical horizontal scale of the measurements being approximately 2.4 km. Data from the standalone FCDP probe are not available for the flights on 16 February and 11 March, so for these flights the data from the Hawkeye FCDP are used.

During each 15 s period,  $\sigma$  was calculated from the combined cloud particle measurements using the projected area [Mitchell, 2002; Mitchell et al., 2011; Schumann et al., 2011] of spheres of bin center diameter for the FCDP data and the imaged particle projected area for the 2-D-S as

$$\sigma = 2 \left( \sum_i n_i \pi (D_i/2)^2 W_i + \sum_j A_j W_j \right) \quad (2)$$

where  $n_i$  is the concentration of particles in an FCDP bin in  $\text{L}^{-1} \mu\text{m}^{-1}$ ,  $D_i$  is the center diameter of the FCDP bin in millimeters,  $A_j$  is the total measured projected area in a 2-D-S bin in  $\text{mm}^2 \text{ L}^{-1} \mu\text{m}^{-1}$ , and  $W$  is the width of the corresponding FCDP or 2-D-S bin in micrometers. The factor of 2 relating  $\sigma$  to  $A$  is the geometric approximation valid for wavelengths that are short relative to the particle dimension,  $\pi D_p/\lambda \gg 1$ .

Issues with determining  $\sigma$  from small ice particles using the FCDP arise from the optical forward scattering nature of the measurement, which is potentially affected by systematic as well as random errors in sizing due to the variable optical properties of ice particles that are a complex function of particle shape, crystal habit, surface roughness and orientation in the detector [Gayet et al., 1996; Borrmann et al., 2000; Yang et al., 2003; Cotton et al., 2010; Nousiainen et al., 2011; Protat et al., 2011; Um and McFarquhar, 2011; Gerber and DeMott, 2014]. All of these factors can alter the amount of light scattered by the particle into the probe detection angles, resulting in an inaccurate estimation of the particle scattering cross section and size since these are calculated from the detected light intensity using Mie theory assuming the particles are smooth spheres. Since the FCDP only provides an estimate of particle size, there is also the need to assume a shape for the particles in order to calculate projected area and  $\sigma$ .

An examination of the CPI images of TTL cirrus ice particles indicates that habits were dominated by compact quasi-spherical and irregular shapes, with a very low incidence of identifiable faceted habits. The aspect ratio of individual particles with maximum dimension 30–50  $\mu\text{m}$  imaged by the CPI was calculated by dividing the particle width by length. The mean value of the aspect ratio across this size range was 0.90 with a standard deviation of 0.08. An estimate of the maximum error introduced by assuming a spherical shape for these

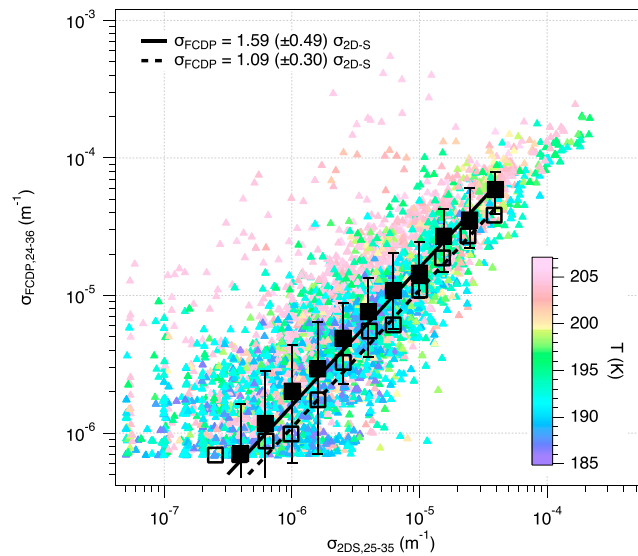


**Figure 2.** Plot of  $\sigma$  calculated from the FCDP bins from 24 to 36  $\mu\text{m}$  versus  $\sigma$  derived from the area in the 2-D-S 15–25  $\mu\text{m}$  bin. The FCDP  $\sigma$  has been scaled by 10/12 to account for the difference in size range. The solid black squares are the median value of  $\sigma_{\text{FCDP},24-36}$  in 0.2  $\log(\sigma_{2\text{D-S},15-25})$  bins, and the error bars denote the interquartile range. A linear fit to the median values yielded a slope of 1.59 indicating the FCDP systematically produced a higher  $\sigma$ . The hollow squares are the median values in each bin considering only data points where the fractional contribution to the total  $\sigma$  was greater than 0.5. The 1.09 slope of the linear fit to these values indicates better agreement between the measurements under these conditions.

particles in the calculation of  $\sigma$  was determined by comparing the reported area for each particle to the projected area calculated for a sphere of the particle maximum dimension (length). The mean value of the ratio was  $0.82 \pm 0.08$ , suggesting an overestimation of projected area and  $\sigma$  from the assumption of spherical shape of  $\sim 22\%$ . Using the average of length and width from the images for the diameter of the sphere produces better agreement with a mean ratio of  $0.90 \pm 0.08$ . A similar calculation comparing the reported area in the 2-D-S 25–35  $\mu\text{m}$  and 35–45  $\mu\text{m}$  size bins for each 15 s measurement period to the projected area calculated assuming the particles were all 30 or 40  $\mu\text{m}$  (bin center) diameter spheres produced a mean value of  $0.90 \pm 0.12$ . Assuming a similar relationship holds for smaller particles, this result suggests a possible systematic overestimation of  $\sim 11\%$  in the contribution to  $\sigma$  from particles  $< 25 \mu\text{m}$  would occur from treating the small ice particles as spheres.

The combined effect from the assumption of spherical shape and from errors in the sizing of ice particles by the FCDP on the calculation of  $\sigma$  can be further evaluated by comparing  $\sigma$  calculated from particles in the FCDP bins from 24 to 36  $\mu\text{m}$  ( $\sigma_{\text{FCDP},24-36}$ ) with that derived from the reported area in the 25–35  $\mu\text{m}$  2-D-S bin ( $\sigma_{2\text{D-S},25-35}$ ). A plot of  $\sigma_{\text{FCDP},24-36}$  versus  $\sigma_{2\text{D-S},25-35}$  is shown in Figure 2. The  $\sigma_{\text{FCDP},24-36}$  data are scaled by 10/12 to account for the difference in the size ranges between the FCDP and 2-D-S. A linear fit of median values of  $\sigma_{\text{FCDP},24-36}$  in 0.2  $\log(\sigma_{2\text{D-S},25-35})$  bins for all data produces a slope of 1.59, indicating the FCDP data typically yield a 60% higher  $\sigma$  than the 2-D-S for this size range. This value is larger than the ratios found above considering sphericity alone, suggesting a systematic effect from particle shape on the FCDP sizing. When only data where the fractional contribution to the total  $\sigma$  from the FCDP is 0.5 or higher, i.e., when the PSD is shifted toward smaller particles, the linear fit produces a slope of 1.09, suggesting improved agreement. This change in the relationship between the FCDP and 2-D-S is due to a greater decrease in the particle concentration measured by the FCDP in the 24–36  $\mu\text{m}$  size range than that measured by the 2-D-S in the 25–35  $\mu\text{m}$  bin. An overall uncertainty in the calculated  $\sigma$  is difficult to quantify with a global number given the large sample to sample variations in effects from counting statistics, size distribution, and particle shape on the measurements.

An additional evaluation of the cloud probe data treatment can be made by comparing the IWC derived from the combined size distributions measured by the cloud probes ( $\text{IWC}_{\text{PSD}}$ ) with the directly measured IWC.  $\text{IWC}_{\text{PSD}}$  is calculated analogously to  $\sigma$  (equation (2)), using the mass reported for the 2-D-S [Baker and Lawson, 2006] for particle sizes  $> 25 \mu\text{m}$  and calculated from the FCDP concentrations by assuming spheres of bin center diameter with density  $0.92 \text{ g cm}^{-3}$  for smaller particles. The calculated mass for individual 15 s measurement periods is shown plotted against the directly measured IWC in Figure 3. There is significant scatter in the distribution across the range, with interquartile ranges similar in magnitude to the median values, increasing to a factor of 3 higher at the lowest IWC. The overall correlation between  $\text{IWC}_{\text{PSD}}$  and IWC is  $r^2 = 0.51$ . A fit to median values of  $\text{IWC}_{\text{PSD}}$  in 0.2  $\log(\text{IWC})$  bins yields a slope of  $0.753 (\pm 0.176)$ , implying that the  $\text{IWC}_{\text{PSD}}$  is systematically lower than the directly measured IWC by 25%, quite reasonable agreement given the uncertainties. Considering those data where the FCDP fractional contribution to  $\sigma$  is greater than

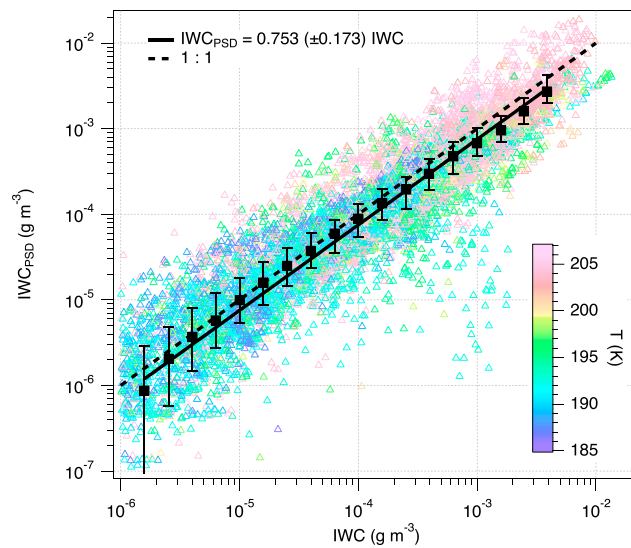


**Figure 3.** IWC calculated from the cloud probe PSD versus directly measured IWC for individual 15 s measurement periods within clouds, colored by temperature. Black squares are median values of  $IWC_{PSD}$  in 0.2 log(IWC) bins, and the error bars denote the interquartile range observed in each bin. The solid black line is a linear fit to the median values indicating that the PSD-derived IWC is systematically ~75% of the directly measured value.

profiles, up to just below the cold point tropopause (typically between 16.5 and 17.5 km). Cloud temperatures ranged from 185 K to 207 K with temperature decreasing with altitude (Figure 1, bottom) following the lapse rate in the TTL. The cirrus encountered had a range of vertical extents from a few hundred meters to >3 km, and cloud bases from above 16 km to below the 14.3 km sampling floor. Relative humidity with respect to ice ( $RH_{ice}$ ) measured within clouds ranged from subsaturated to supersaturated at all temperatures. The median value was near saturation (101%) for temperatures greater than 192 K, while there was an increasing tendency toward supersaturation at colder temperatures. The Global Hawk flight paths avoided proximity to active deep convection, which was widespread throughout the region, and most TTL clouds sampled were between 1 and 10 days removed from the most recent convective influence [Jensen et al., 2016].

Cirrus cloud microphysical properties are a complex function of a number of parameters, including temperature, cooling rate, available water vapor, available ice nuclei, and cloud history [e.g., Jensen et al., 2010; Krämer et al., 2016]. Variability in these parameters leads to significant heterogeneity in IWC, INC, size distribution, and ice habit across a range of spatial scales, both horizontally and vertically, and produces variability in large-scale cloud radiative properties [e.g., Fu et al., 2000; Baran, 2012]. A measure of the cloud heterogeneity is the variation observed in  $\sigma$  and IWC within clouds from one data point to the next. The median 1 s relative change, corresponding to ~160 m horizontal distance and up to 35 m vertical, in  $\sigma$  during cloud sampling was 39%, while that in IWC was 14%. Discretization due to counting statistics at the frequently low INC contributed significantly to the greater relative changes in  $\sigma$ , but the changes in the directly measured IWC are much greater than the measurement precision (typically <2%) and reflect real variability. For the data averaged over 15 s intervals, the median relative changes in  $\sigma$  and IWC were similar at 33% and 29%, respectively, reflecting real changes in cloud properties occurring over the longer measurement intervals. These variations are much larger than the corresponding median 15 s changes in other atmospheric variables such as water vapor (< 3%). This heterogeneity contributes to significant scatter in the observed relationship between IWC and  $\sigma$ .

The IWC- $\sigma$  relationship in cirrus clouds has previously been found to exhibit systematic variations with temperature [Heymsfield et al., 2005; Heymsfield et al., 2006; Mioche et al., 2010; Heymsfield et al., 2014]. A temperature dependence is also observed in the ATTREX data. Figure 4 shows a plot of IWC versus  $\sigma$  for individual 15 s measurements colored by temperature. Aggregating the data for all temperatures, median values for IWC in 0.1 log( $\sigma$ ) bins are shown in the plot along with a least squares power law curve fit to the medians. The 1.01

0.5, the agreement improves to ~20% low, and for intervals where the FCDP fraction of  $\sigma$  is greater than 0.85, the agreement approaches unity. Overall, this finding suggests that the inclusion and treatment of the FCDP data are reasonable for the IWC- $\sigma$  analysis.

### 2.3. Other Measurements

Static temperature and pressure were measured by the Meteorological Measurement System (MMS) [Scott et al., 1990] with uncertainties of  $\pm 0.3$  K and  $\pm 0.5$  hPa, respectively. Additionally, aircraft true air speed derived from the MMS measurements was used for the determination of the particle enhancement factor of the NOAA Water total water inlet.

### 3. Results and Discussion

During ATTREX 2014, TTL cirrus were sampled at altitudes from 14.3 km, the typical bottom of Global Hawk vertical

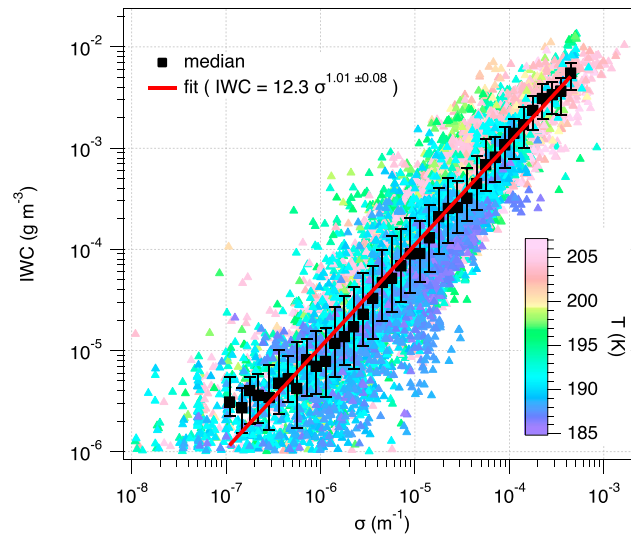


**Figure 4.** IWC versus  $\sigma$  for individual 15 s measurement periods within clouds. The data are colored by temperature, which reveals that at the coldest temperatures ( $T < \sim 189$ ), the clouds typically exhibited a systematically lower IWC for a given  $\sigma$ . Black squares are the median values of IWC in 0.1  $\log(\sigma)$  bins, and the error bars denote the interquartile range observed in each bin. The red line shows a power law fit to the median values which returns an exponential factor of  $1.01 \pm 0.08$ , indicating a nearly linear relationship.

Heymsfield et al., 2006; Mitchell et al., 2011] and is therefore insensitive to INC, leaving it primarily a function of the cloud PSD and ice crystal habit. Using the relationship between cloud particle projected area and  $\sigma$  (equation (1)),  $D_{\text{eff}}$  for the ATTREX data is calculated as

$$D_{\text{eff}} = \frac{3 \text{ IWC}}{\rho_{\text{ice}} \sigma} \tag{3}$$

where IWC is in  $\text{g m}^{-3}$ ,  $\rho_{\text{ice}}$  is the density of pure ice,  $0.92 \text{ g cm}^{-3}$ ,  $\sigma$  is in  $\text{m}^{-1}$ , and  $D_{\text{eff}}$  is in micrometers. The uncertainty in the calculated  $D_{\text{eff}}$  is affected by the uncertainty in calculating  $\sigma$  from the cloud probe measurements given the small particle sizes, low INCs, and the assumptions required to utilize the FCDP data and additionally includes the systematic uncertainty in the direct IWC measurement. The median 15 s relative change in  $D_{\text{eff}}$  is 26% (interquartile range 12%–53%), slightly lower than that for IWC alone, reflecting the covariance of IWC and  $\sigma$ . Significant variations were observed in  $D_{\text{eff}}$  both within individual clouds and between clouds sampled at similar atmospheric conditions, reflecting the complexity of cirrus formation and evolution processes.  $D_{\text{eff}}$  in some clouds was lower near the top of the cloud and increased with distance below cloud top, similar to profiles of  $\text{IWC}/\sigma$  reported by Heymsfield et al. [2005], while others exhibited no significant variation with height and still others included horizontal layers of varying  $D_{\text{eff}}$  within the cloud. Figure 5 shows the distribution of the calculated  $D_{\text{eff}}$  as a function of temperature in 1 K temperature bins. A broad range of values are present at all temperatures, with the distributions being generally lognormal. Cirrus populations at temperatures greater than 192 K exhibited  $D_{\text{eff}}$  distributions centered (median) between 40 and 50  $\mu\text{m}$  with only a weak temperature dependence that can be described by the linear relationship

$$D_{\text{eff}} = 40 + 0.53 (T - 192) \quad T > 192 \text{ K} \tag{4}$$

which reproduces the median values with a relative mean absolute deviation of less than 10%. Below 192 K,  $D_{\text{eff}}$  decreases sharply with decreasing temperature, reaching a median value near 12  $\mu\text{m}$  for  $T < 187$  K. The available data below 186 K is too limited to determine if  $D_{\text{eff}}$  has leveled off or would continue to decrease at even lower temperatures. The decrease in  $D_{\text{eff}}$  at the coldest temperatures indicates a systematic shift of the size distribution toward smaller ice particles since mass decreases faster than cross sectional area with decreasing diameter. Figure 5 shows the mean contribution of different particles sizes to  $\sigma$  for sampled cirrus populations at  $T > 192$  K and for  $T < 189$  K. For the coldest

value of the exponent in the fit indicates that overall, the relationship between IWC and  $\sigma$  in the ATTREX observations is essentially linear. In the plot, it can be seen that clouds at the coldest temperatures ( $T < 189$  K) fall fairly consistently below the median line, indicating they typically have lower IWC values for a given  $\sigma$  than do clouds at warmer temperatures. Among clouds sampled at warmer temperatures, no obvious trend in the distribution as a function of temperature is apparent.

To more closely examine the temperature dependence of the IWC- $\sigma$  relationship in the ATTREX data, the IWC and cloud particle measurements were used to calculate the cloud effective diameter,  $D_{\text{eff}}$ , in each measurement interval.  $D_{\text{eff}}$  is commonly defined as the cloud particle volume divided by the projected area [Foot, 1988; McFarquhar and Heymsfield, 1998; Mitchell, 2002;

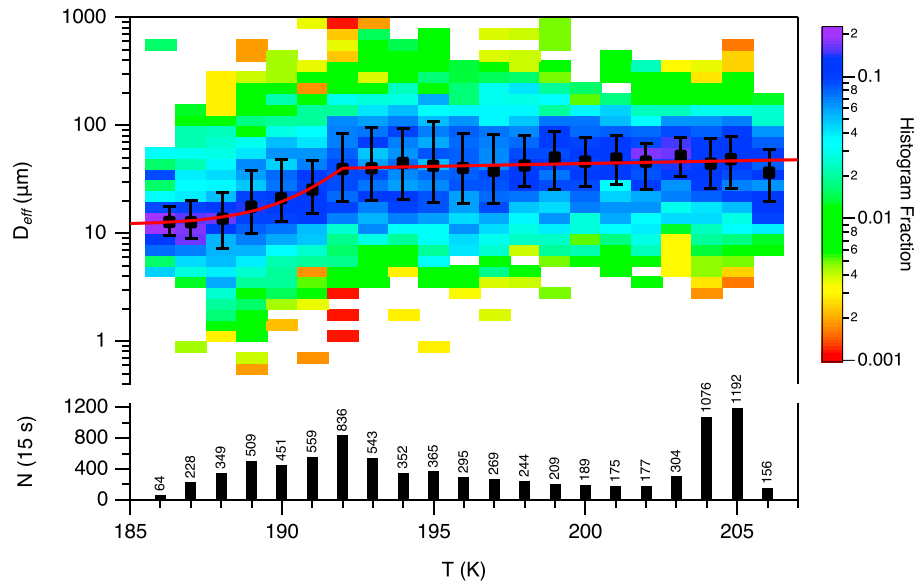


**Figure 5.** Distribution of  $D_{\text{eff}}$  as a function of temperature. Median values in each 1 K bin are indicated by black squares, and error bars indicate the interquartile range. The calculated  $D_{\text{eff}}$  for individual 15 s measurements exhibits a significant range of values at all temperatures. The distributions are centered between 40  $\mu\text{m}$  and 50  $\mu\text{m}$  for cirrus sampled at  $T > 192$  K, decreasing slightly with decreasing temperature, while  $D_{\text{eff}}$  falls more rapidly with decreasing  $T$  below 192 K. The red line shows the segmented fit to the median values. Note the color scale of the distributions is logarithmic. Bars at the bottom of the plot show the number of 15 s measurement periods within cirrus in each temperature bin.

clouds, the  $\sigma$  distribution exhibits a peak near 12  $\mu\text{m}$  diameter, while at warmer temperatures there is a broad peak between 20 and 45  $\mu\text{m}$ , with a significant contribution from particles larger than 45  $\mu\text{m}$ . The decrease in median  $D_{\text{eff}}$  below 192 K is reasonably well represented by an exponential fit

$$D_{\text{eff}} = 12 + 28 e^{0.65(T-192)} \quad T < 192 \text{ K} \quad (5)$$

which reproduces the median values with a relative mean absolute deviation of 5%. The derived parameterization of  $D_{\text{eff}}(T)$  across the full temperature range is shown as the red line in Figure 5.

It is worth noting that near the point where the transition between the two temperature regions occurs, there is also a shift in the relative contributions to  $\sigma$  from the FCDP and 2-D-S probes as the PSD shifts toward smaller sizes with decreasing temperature. This transition is apparent in the plot in Figure 6, which shows the distribution of the fractional contribution to  $\sigma$  from the FCDP measurement in 1 K temperature bins.

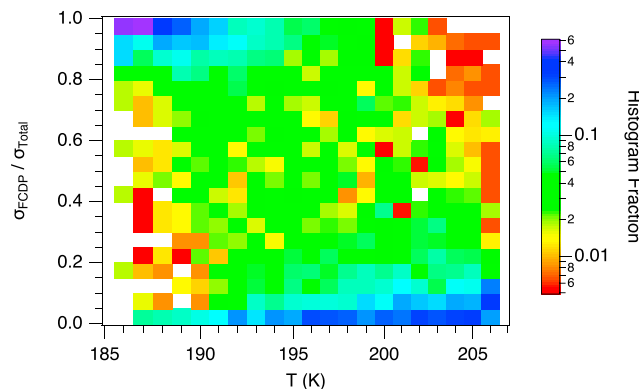


**Figure 6.** Distribution of the fractional contribution of the FCDP-derived  $\sigma$  from particle sizes 1–25  $\mu\text{m}$  to the total  $\sigma$  ( $\sigma_{\text{FCDP}}/\sigma_{\text{Total}}$ ) as a function of temperature. An increase in the relative contribution from the FCDP at colder temperatures is consistent with a shift of the size distributions toward smaller sizes.

That the derived shape of  $D_{\text{eff}}(T)$  is not an artifact created by combining the two measurements is confirmed by the fact that a similar transition is observed in both instruments independently, although attenuated in the 2-D-S due to the larger minimum detectable particle size, and with appreciably greater scatter in the FCDP due to the poor counting statistics in the larger size bins. As can be seen in Figure 6, for temperatures  $< 189$  K,  $\sigma$  was frequently determined almost entirely by particles  $< 25$   $\mu\text{m}$ . The shift in  $\sigma$  to smaller particles at

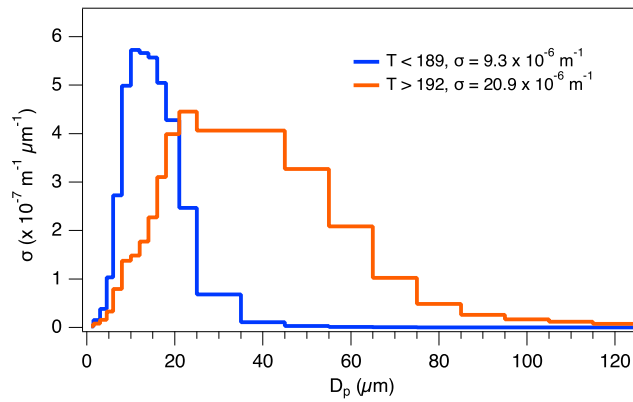


**Figure 7.** Distribution of  $\sigma$  as a function of particle size for cirrus sampled at the coldest temperatures encountered ( $T < 189$  K) and clouds sampled at warmer temperatures ( $T > 192$  K). The shift to smaller particles at the coldest temperatures is apparent, with the peak in the  $\sigma$  distribution occurring below  $15 \mu\text{m}$  while at warmer temperatures the distribution exhibits a broad peak between  $25$  and  $45 \mu\text{m}$ . The median total extinction for  $T < 189$  K is only  $\sim 2$  lower than the value at higher temperatures.

by red squares, with error bars denoting the interquartile range of the distribution in each bin. The median values of cIWC/mIWC are within 10% of unity for  $\sigma > 2 \times 10^{-6} \text{ m}^{-1}$  but exhibit larger deviations at lower  $\sigma$ . These deviations largely arise from measurement limitations as the discretization of the cloud probe measurements becomes more significant in optically very thin cirrus and the low IWC of the clouds more frequently falls below the detection limit of the NOAA Water instrument, skewing the remaining distribution. These effects are also visible at the lowest  $\sigma$  values in the plot of IWC versus  $\sigma$  shown in Figure 4.

The ratio of the individual 15 s cIWC values to the corresponding mIWC exhibits a broad range due to the heterogeneity of cloud properties and scatter in the measurements. Figure 9 shows the PDF of the cIWC/mIWC ratios for all of the ATTREX data. The median value of the ratio is 0.99, and the distribution of the ratios is lognormal centered at 1.01, with 56% of the individual ratios falling within a factor of 2 and 85% within a factor of 4 of unity. This distribution provides a reasonable estimate for the overall uncertainty in the application of derived parameterization for individual measurements of  $\sigma$ .

The IWC- $\sigma$  parameterization derived from the ATTREX data is plotted in Figure 10 along with parameterizations for cold cirrus reported in the literature and included in Table 1. From the plot, it can be seen that the  $D_{\text{eff}}$  parameterization of the ATTREX data has a lower slope than the temperature-independent power law

the coldest temperatures is further illustrated by the differences between the  $\sigma$  distributions as a function of cloud particle size for cold and warm clouds shown in Figure 7.

The  $D_{\text{eff}}(T)$  parameterization is used to calculate IWC from the measured  $\sigma$  by inverting equation (3) to solve for IWC as a function of  $D_{\text{eff}}$  and  $\sigma$ . The calculated IWC (cIWC) can then be compared to the directly measured IWC (mIWC) to assess the parameterization and its associated error. Figure 8 shows a plot of the ratio of cIWC to mIWC for individual 15 s measurements as a function of the measured  $\sigma$ . Median values of the ratio in  $0.1 \log(\sigma)$  bins are indicated

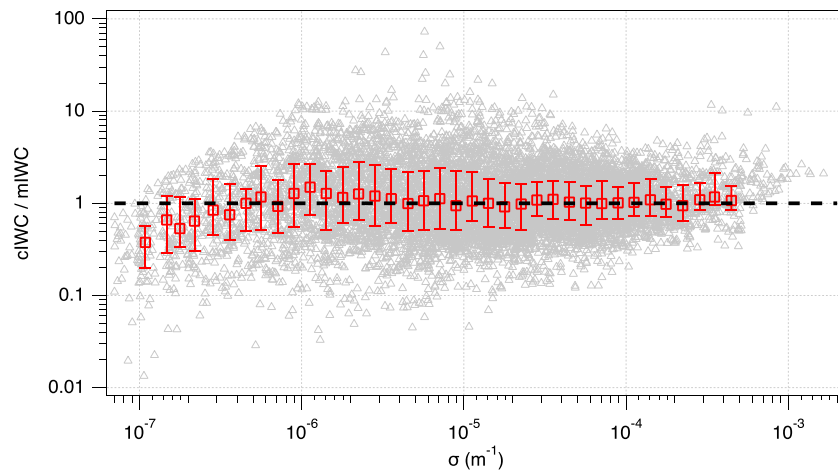


**Figure 8.** Plot of the ratio of calculated IWC using the ATTREX  $D_{\text{eff}}(T)$  parameterization to directly measured IWC (cIWC/mIWC) for individual 15 s measurement periods as a function of the measured  $\sigma$ . The red squares are the median values of the distributions in  $0.1 \log(\sigma)$  bins and the error bars describe the interquartile range. The dashed line is 1.

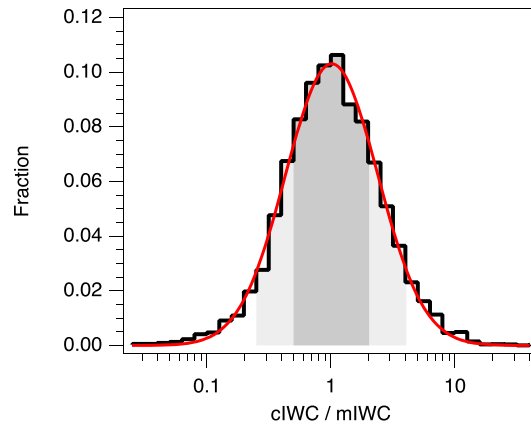


**Figure 9.** PDF of individual 15 s ratios of the calculated IWC to measured IWC (clWC/mlWC). The distribution of the ratios is lognormal (red curve) around 1, with 56% of individual values within a factor of two (dark grey shading) and 85% within a factor of 4 (light grey shading).

parameterization,  $IWC = 119\sigma^{1.22}$ , reported by *Heymsfield et al.* [2005, H05], which was used to produce the CALIOP version 3, Level 2 IWC product. For cirrus at 188 K, the H05 parameterization yields IWC higher than the ATTREX parameterization by a factor of 1.5 to 5 as  $\sigma$  increases from  $10^{-6}$  to  $5 \times 10^{-4} \text{ m}^{-1}$ . At  $T = 198 \text{ K}$ , H05 produces IWC values that range from a factor of 2 lower to a factor of 1.7 higher over the same  $\sigma$  range. *Avery et al.* [2012] reported distributions of IWC calculated from CALIOP measurements using both the H05 parameterization and H05 multiplied by a factor of 2 to account for large particle shattering and a potential underestimate at cold temperatures suggested by a ground-based radar-lidar comparison [*Protat et al.*, 2010]. This modified parameterization leads to calculated IWC significantly higher than ATTREX at all  $\sigma$  for 188 K, and for all but the lowest  $\sigma$  at 198 K.

*Heymsfield et al.* [2014, H14] performed an extensive analysis of IWC and cloud probe data from a number of field campaigns, including data from the tropical TTL at temperatures down to 187 K. More of the cold tropical cirrus data in their analysis was of recent convective (anvil) outflow than was encountered during ATTREX but

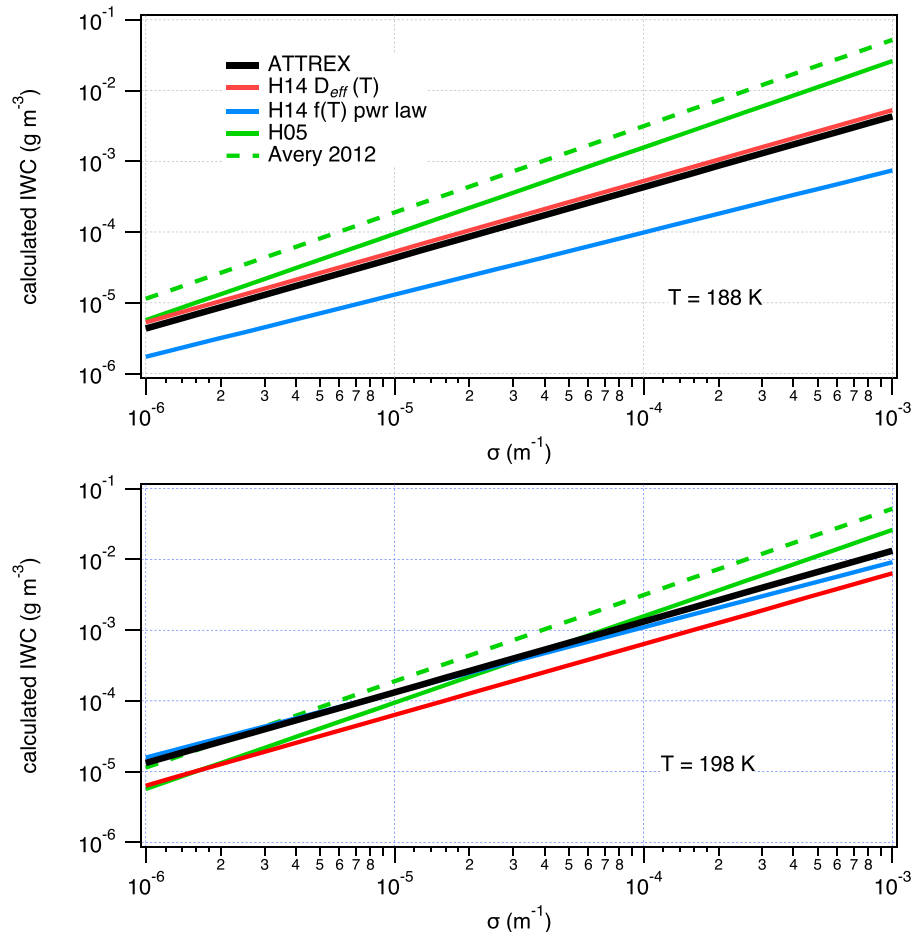


**Figure 10.** Comparison of IWC- $\sigma$  relationships from the ATTREX 2014 analysis with literature parameterizations for cirrus clouds at (top) 188 K and (bottom) 198 K.

Parameterization	T Range	Source
$IWC = 119\sigma^{1.22}$	198–263 K	Heymsfield et al. [2005]
$IWC = 238\sigma^{1.22}$		Avery et al. [2012]
$IWC = a\sigma^b$ $a = 0.00532(T - 183)^{2.55}, b = 1.31e^{(0.0047(T-273))}$	188–270 K	Heymsfield et al. [2014]
$IWC = \sigma (0.91/3) (9.1744 \times 10^4 e^{0.117(T-273)})$ $= \sigma (0.91/3) (83.3 e^{0.0184(T-273)})$	202–217 K 188–202 K	Heymsfield et al. [2014]
$IWC = (0.92/3) (40 + 0.53 (T - 192))$ $= (0.92/3) (12 + 28e^{0.65(T-192)}) \sigma$	192–207 K 185–192 K	This work

included data from several regions and seasons. Much of the cold cirrus data rely on a gamma function to parameterize the small particle size distribution due to potential artifacts and other issues with those measurements. From the aggregated data, they derive both a power law parameterization with temperature-dependent coefficients (H14, equation (9d)) and a  $D_{eff}(T)$  parameterization (H14, equation (9e)) that they suggest perform well in the temperature range 187–213 K that encompasses all but the coldest of the ATTREX data. The H14  $D_{eff}(T)$  parameterization is under consideration for the CALIOP version 4, Level 2 IWC product (M. Avery, private communication, 2016). From Figure 10 it can be seen that the temperature-dependent power law parameterization yields an IWC that is a factor of 2–5 lower than the ATTREX parameterization at 188 K but agrees within  $\pm 30\%$  at 198 K. The definition of  $D_{eff}$  (equation (3)) results in a linear relationship between IWC and  $\sigma$ , so the H14 and ATTREX  $D_{eff}(T)$  parameterizations produce parallel estimates of IWC from  $\sigma$  that differ by a constant value for a given temperature. At 188 K, the two lines are similar, with H14 lying slightly above the ATTREX value, while at 198 K the H14 values are lower than the ATTREX parameterization. Figure 11 shows a more direct comparison of the H14 and ATTREX-derived  $D_{eff}(T)$  parameterizations, plotting the calculated IWC for  $\sigma = 1 \times 10^{-6} \text{ m}^{-1}$  over the temperature range 185–207 K. In contrast to the ATTREX  $D_{eff}(T)$ , the H14 parameterization exhibits a slow increase in  $D_{eff}$  with temperature at  $T < 202$  K, followed by a more rapid increase above that. The difference between the parameterization is roughly a factor of 2 between 192 and 202 K, but smaller at both colder and warmer temperatures. Applying the H14  $D_{eff}(T)$  parameterization to the ATTREX data results in a systematic 1/3 underestimation of the median measured IWC across the range of observed  $\sigma$ , and the calculated IWC would therefore need to be scaled by 1.5 to best match the ATTREX observations.

#### 4. Summary and Conclusions

Given the prevalence of thin cirrus clouds in the TTL and their significance in Earth’s radiation budget, the ability to accurately model their properties is important in order to predict their role as a feedback in response

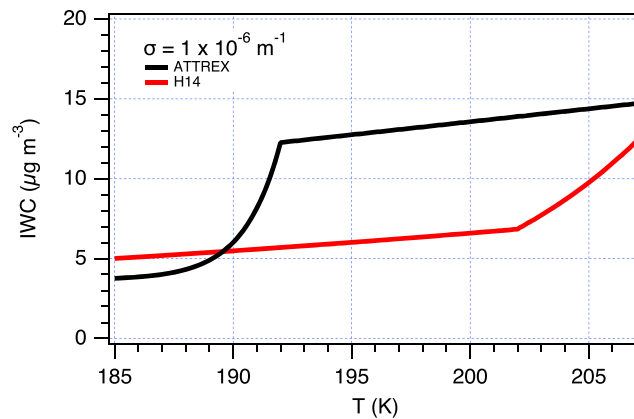


**Figure 11.** Comparison of IWC as a function of  $T$  calculated for constant  $\sigma = 1 \times 10^{-6} \text{ m}^{-1}$  using the ATTREX parameterization (black line) with that from the  $D_{eff}(T)$  parameterization reported in Heymsfield et al. [2014, H14] (red line).

to changes in climate. IWC and effective diameter are important parameters for determining the radiative properties of clouds and useful metrics by which the treatment of cirrus clouds in global climate models can be compared to observations. For TTL cirrus, the best observations for comparison are from space-based lidars such as CALIOP that can provide both long-term and large spatial coverage. However, in order to compare the model IWC to lidar extinction retrievals for thin tropical cirrus, an accurate parameterization relating extinction to IWC is needed. For cold TTL cirrus, relationships that are extrapolated from midlatitude cirrus or warmer

temperatures may not be appropriate, since formation mechanisms and environmental conditions are different in the TTL.

The in situ IWC and cloud microphysical measurements from the ATTREX mission in the western tropical Pacific provide an extensive data set by which the IWC- $\sigma$  relationship can be evaluated for this important region. The cold TTL cirrus sampled exhibited a very low incidence of large ice particles, and no evidence of shattering-induced artifact in the small particle size range was detected, allowing inclusion of the small particle data in the determination of  $\sigma$ . This was especially important at the coldest temperatures where the mode of the size distribution was frequently below 15  $\mu\text{m}$ . The low 1  $\mu\text{g m}^{-3}$  detection limit of the IWC measurement during ATTREX allows the analysis to be extended to optically thinner clouds than have been reported previously using direct IWC measurements.

The ATTREX TTL cirrus data, spanning an altitude range of 14.3–17.3 km and temperatures from 185 to 207 K indicate that  $D_{\text{eff}}$  was in the range of 40–50  $\mu\text{m}$  for  $T > 192$  K and exhibited only a slight decrease from 207 K down to 192 K. Below 192 K,  $D_{\text{eff}}$  decreased sharply with decreasing temperature to a value near 12  $\mu\text{m}$  at 186 K. From the derived  $D_{\text{eff}}(T)$  parameterization, very cold cirrus sampled at  $T < 189$  K typically have only ~30% of the IWC for a given  $\sigma$  as warmer clouds sampled at  $T > 192$  K. This is supported by the observation that the size distribution shifted toward smaller particles at colder temperatures.

The IWC- $\sigma$  relationship derived from the ATTREX data differs from the parameterizations based on measurements from a number of previous aircraft campaigns in cold cirrus and will result in differences of up to a factor of 2 in the IWC calculated from extinction in TTL cirrus. This would impact IWC reported from optical probe and lidar measurements in the TTL that are a primary tool for assessment and constraint of cloud parameterization in climate models. Additional measurements of TTL cirrus properties in different regions and seasons, and down to even colder temperatures than were reached during ATTREX, would be useful to assess and extend the generalizability of these results.

#### Acknowledgments

The authors would like to thank the ground and flight crews of the NASA Global Hawk for their efforts during the ATTREX campaign. Funding for this work was provided by the NASA Airborne Tropical Tropopause Experiment, the NASA Radiation Sciences Program, the NASA Upper Atmosphere Research Program, and the NOAA Climate Program Office. The 2014 ATTREX data used in this analysis are publicly available in the NASA ESPO Data Archive at <https://espoarchive.nasa.gov/archive/browse/attrex/id4>.

#### References

- Avery, M., D. Winker, A. Heymsfield, M. Vaughan, S. Young, Y. Hu, and C. Trepte (2012), Cloud ice water content retrieved from the CALIOP space-based lidar, *Geophys. Res. Lett.*, *39*, L05808, doi:10.1029/2011GL05045.
- Baker, B., and R. P. Lawson (2006), Improvement in determination of ice water content from two-dimensional particle imagery. Part I: Image-to-mass relationships, *J. Appl. Meteorol. Climatol.*, *45*, 1282–1290.
- Baran, A. J. (2012), From the single-scattering properties of ice crystals to climate prediction: A way forward, *Atmos. Res.*, *112*, 45–69, doi:10.1016/j.atmosres.2012.04.010.
- Borrmann, S., B. Luo, and M. Mishchenko (2000), Application of the T-Matrix method to the measurement of aspherical (ellipsoidal) particles with forward scattering optical particle counters, *J. Aerosol Sci.*, *31*, 789–799, doi:10.1016/S0021-8502(99)00563-7.
- Bretherton, C. S. (2015), Insights into low-latitude cloud feedbacks from high-resolution models, *Phil. Trans. R. Soc. A*, *373*, 20140415, doi:10.1098/rsta.2014.0415.
- Comstock, J. M., T. P. Ackerman, and G. G. Mace (2002), Ground-based lidar and radar remote sensing of tropical cirrus clouds at Nauru Island: Cloud statistics and radiative impacts, *J. Geophys. Res.*, *107*(D23), 4714, doi:10.1029/2002JD002203.
- Cotton, R., S. Osborne, Z. Ulanowski, E. Hirst, P. H. Kaye, and R. S. Greenaway (2010), The ability of the small ice detector (SID-2) to characterize cloud particle and aerosol morphologies obtained during flights of the FAAM Bae-146 research aircraft, *J. Atmos. Ocean. Technol.*, *27*, 290–303, doi:10.1175/2009JTECHA1282.1.
- Davis, S. M., L. M. Avallone, E. M. Weinstock, C. H. Twohy, J. B. Smith, and G. L. Kok (2007), Comparisons of in situ measurements of cirrus cloud ice water content, *J. Geophys. Res.*, *112*, D10212, doi:10.1029/2006JD008214.
- Donovan, D. P., and A. C. A. P. van Lammeren (2001), Cloud effective particle size and water content profile retrievals using combined lidar and radar observations: 1. Theory and examples, *J. Geophys. Res.*, *106*, 27,425–27,448, doi:10.1029/2001JD900243.
- Eddy, P., A. Natarajan, and S. Dhaniyala (2006), Subisokinetic sampling characteristics of high speed aircraft inlets: A new CFD-based correlation considering inlet geometries, *J. Aerosol Sci.*, *37*, 1853–1870, doi:10.1016/j.jaerosci.2006.08.005.
- Foot, J. S. (1988), Some observations of the optical properties of clouds. II: Cirrus, *Q. J. R. Meteorol. Soc.*, *114*, 145–164, doi:10.1002/qj.49711447908.
- Fu, Q., B. Carlin, and G. Mace (2000), Cirrus horizontal inhomogeneity and OLR bias, *Geophys. Res. Lett.*, *27*, 3341–3344, doi:10.1029/2000GL011944.
- Fueglistaler, S., A. E. Dessler, T. J. Dunkerton, I. Folkins, Q. Fu, and P. W. Mote (2009), Tropical tropopause layer, *Rev. Geophys.*, *47*, RG1004, doi:10.1029/2008RG000267.
- Gayet, J.-F., G. Febvre, and H. Larsen (1996), The reliability of the PMS FSSP in the presence of small ice crystals, *J. Atmos. Ocean. Technol.*, *13*, 1300–1310, doi:10.1175/1520-0426(1996)013<1300:TROTPF>2.0.CO;2.
- Gerber, H., and P. J. DeMott (2014), Response of FSSP-100 and PVM-100A to small ice crystals, *J. Atmos. Ocean. Technol.*, *31*, 2145–2155, doi:10.1175/JTECH-D-13-00228.1.
- Heymsfield, A. J. (2007), On measurements of small ice particles in clouds, *Geophys. Res. Lett.*, *34*, L23812, doi:10.1029/2007GL030951.
- Heymsfield, A. J., D. Winker, and G. van Zadelhoff (2005), Extinction-ice water content-effective radius algorithms for CALIPSO, *Geophys. Res. Lett.*, *32*, L10807, doi:10.1029/2005GL022742.
- Heymsfield, A. J., C. Schmitt, A. Bansemmer, M. J. McGill, C. Twohy, and D. Baumgardner (2006), Effective radius of ice cloud particle populations derived from aircraft probes, *J. Atmos. Ocean. Technol.*, *23*, 361–380, doi:10.1175/JTECH1857.1.

- Heymsfield, A. J., D. Winker, M. Avery, M. Vaughan, G. Diskin, M. Deng, V. Mitev, and R. Matthey (2014), Relationships between ice water content and volume extinction coefficient from in situ observations for temperatures from 0° to −86°C: Implications for spaceborne lidar retrievals, *J. Appl. Meteorol. Climatol.*, *53*, 479–505, doi:10.1175/JAMC-D-13-087.1.
- Jensen, E. J., and L. Pfister (2004), Transport and freeze-drying in the tropical tropopause layer, *J. Geophys. Res.*, *109*, D02207, doi:10.1029/2003JD004022.
- Jensen, E. J., et al. (2009), On the importance of small ice crystals in tropical anvil cirrus, *Atmos. Chem. Phys.*, *9*, 5519–5537, doi:10.5194/acp-9-5519-2009.
- Jensen, E. J., L. Pfister, T.-P. Bui, P. Lawson, and D. Baumgardner (2010), Ice nucleation and cloud microphysical properties in tropical tropopause layer cirrus, *Atmos. Chem. Phys.*, *10*, 1369–1384, doi:10.5194/acp-10-1369-2010.
- Jensen, E. J., et al. (2016), The NASA Airborne Tropical Tropopause Experiment (ATTREX): High-altitude aircraft measurements in the tropical western Pacific, *Bull. Am. Meteorol. Soc.*, *98*, 129–143, doi:10.1175/BAMS-D-14-00263.1.
- Korolev, A. V., E. F. Emery, J. W. Strapp, S. G. Cober, and G. A. Isaac (2013), Quantification of the effects of shattering on airborne ice particle measurements, *J. Atmos. Ocean. Technol.*, *30*, 2527–2553, doi:10.1175/JTECH-D-13-00115.1.
- Korolev, A., and P. R. Field (2015), Assessment of the performance of the inter-arrival time algorithm to identify ice shattering artifacts in cloud particle probe measurements, *Atmos. Meas. Tech.*, *8*, 761–777, doi:10.5194/amt-8-761-2015.
- Krämer, M., et al. (2016), A microphysics guide to cirrus clouds—Part 1: Cirrus types, *Atmos. Chem. Phys.*, *16*, 3463–3483, doi:10.5194/acp-16-3463-2016.
- Lance, S., C. A. Brock, D. Rogers, and J. A. Gordon (2010), Water droplet calibration of the Cloud Droplet Probe (CDP) and in-flight performance in liquid, ice and mixed-phase clouds during ARCPAC, *Atmos. Meas. Tech.*, *3*, 1683–1706, doi:10.5194/amt-3-1683-2010.
- Lawson, R. P. (2011), Effects of ice particles shattering on the 2D-S probe, *Atmos. Meas. Tech.*, *4*, 1361–1381, doi:10.5194/amt-4-1361-2011.
- Lawson, R. P., D. O'Connor, P. Zmarzly, K. Weaver, B. A. Baker, Q. Mo, and H. Jonsson (2006), The 2D-S (Stereo) probe: Design and preliminary tests of a new airborne, high-speed, high-resolution particle imaging probe, *J. Atmos. Ocean. Technol.*, *23*, 1462–1477.
- Li, J.-L. F., et al. (2012), An observationally based evaluation of cloud ice water in CMIP3 and CMIP5 GCMs and contemporary reanalyses using contemporary satellite data, *J. Geophys. Res.*, *117*, D16105, doi:10.1029/2012JD017640.
- Luebke, A. E., L. M. Avallone, C. Schiller, J. Meyer, C. Rolf, and M. Krämer (2013), Ice water content of Arctic, Midlatitude, and tropical cirrus—Part 2: Extension of the database and new statistical analysis, *Atmos. Chem. Phys.*, *12*, 6447–6459, doi:10.5194/acp-12-6447-2013.
- Massie, S. T., J. Gille, C. Craig, R. Khosravi, J. Barnett, W. Read, and D. Winker (2010), HIRDLS and CALIPSO observations of tropical cirrus, *J. Geophys. Res.*, *115*, D00H11, doi:10.1029/2009JD012100.
- McFarquhar, G. M., and A. J. Heymsfield (1998), Microphysical characteristics of three anvils sampled during the Central Equatorial Pacific Experiment, *J. Atmos. Sci.*, *53*(17), 2401–2423, doi:10.1175/1520-0469(1998)053<2401:MCOTAS>2.0.CO;2.
- McFarquhar, G. M., J. Um, M. Freer, D. Baumgardner, G. L. Kok, and G. Mace (2007), Importance of small ICE crystals to cirrus properties, observations from the Tropical Warm Pool International Cloud Experiment (TWP-ICE), *Geophys. Res. Lett.*, *34*, L13803, doi:10.1029/2007GL029865.
- Mioche, G., D. Jossset, J.-F. Gayet, J. Pelon, A. Garnier, A. Minikin, and A. Schwarzenboeck (2010), Validation of the CALIPSO-CALIOP extinction coefficients from in situ observations in midlatitude cirrus clouds during the CIRCLE-2 experiment, *J. Geophys. Res.*, *115*, D00H25, doi:10.1029/2009JD012376.
- Mitchell, D. L. (2002), Effective diameter in radiation transfer: General definition, applications, and limitations, *J. Atmos. Sci.*, *59*, 2330–2346, doi:10.1175/1520-0469(2002)059<2330:EDIRTG>2.0.CO;2.
- Mitchell, D. L., R. P. Lawson, and B. Baker (2011), Understanding effective diameter and its application to terrestrial radiation in ice clouds, *Atmos. Chem. Phys.*, *11*, 3417–3429, doi:10.5194/acp-11-3418-2011.
- Nousiainen, T., H. Lindqvist, G. M. McFarquhar, and J. Um (2011), Small irregular ice crystals in tropical cirrus, *J. Atmos. Sci.*, *68*, 2614–2627, doi:10.1175/2011JAS3733.1.
- O'Connor, D., B. Baker, and R. P. Lawson (2008), Upgrades to the FSSP-100 electronics, 15th. Int. Conf. on Clouds and Precipitation. Cancun, Mexico, Univ. Nacional Autonomy de México, P13.6. [Available at [http://cabernet.atmosfcu.unam.mx/ICCP-2008/abstracts/Program\\_on\\_line/Poster\\_13/O'Connor\\_extended.pdf](http://cabernet.atmosfcu.unam.mx/ICCP-2008/abstracts/Program_on_line/Poster_13/O'Connor_extended.pdf)]
- Protat, A., J. Delanoë, E. J. O'Connor, and T. S. L'Ecuyer (2010), The evaluation of CloudSat and CALIPSO ice microphysical products using ground-based cloud radar and lidar observations, *J. Atmos. Ocean. Technol.*, *27*, 793–810, doi:10.1175/2009JTECHA1397.1.
- Protat, A., G. M. McFarquhar, J. Um, and J. Delanoë (2011), Obtaining best estimates for the microphysical and radiative properties of tropical ICE clouds from TWP-ICE in situ microphysical observations, *J. Appl. Meteorol. Climatol.*, *50*, 895–915, doi:10.1175/2010JAMC2401.1.
- Randel, W. R., and E. J. Jensen (2013), Physical processes in the tropical tropopause layer and their roles in a changing climate, *Nat. Geosci.*, *6*, 169–176, doi:10.1038/NCEO1733.
- Sassen, K., Z. Wang, and D. Liu (2008), Global distribution of cirrus clouds from CloudSat/Cloud-Aerosol Lidar and Infrared Pathfinder Satellite Observations (CALIPSO) measurements, *J. Geophys. Res.*, *113*, D00A12, doi:10.1029/2008JD009972.
- Schumann, U., B. Mayer, K. Gierens, S. Unterstrasser, P. Jessberger, A. Petzold, and C. Voigt (2011), Effective radius of ice particles in cirrus and contrails, *J. Atmos. Sci.*, *68*, 300–321, doi:10.1175/2010JAS3562.1.
- Scott, S. G., T. P. Bui, K. R. Chan, and S. W. Bowen (1990), The meteorological measurement system on the NASA ER-2 aircraft, *J. Atmos. Ocean. Technol.*, *7*(4), 525–540, doi:10.1175/1520-0426(1990)007<0525:TMMSSOT>2.0.CO;2.
- Thornberry, T. D., A. W. Rollins, R. S. Gao, L. A. Watts, S. J. Ciciora, R. J. McLaughlin, and D. W. Fahey (2015), A two-channel, tunable diode laser-based hygrometer for measurement of water vapor and cirrus cloud ice water content in the upper troposphere and lower stratosphere, *Atmos. Meas. Tech.*, *8*, 211–224, doi:10.5194/amt-8-211-2015.
- Um, J., and G. M. McFarquhar (2011), Dependence of the single-scattering properties of small ice crystals on idealized shape models, *Atmos. Chem. Phys.*, *11*, 3159–3171, doi:10.5194/acp-11-3159-2011.
- van Zadelhoff, G.-J., A. J. Heymsfield, D. P. Donovan, and M. J. McGill (2007), Evaluating lidar-radar microphysics retrieval using in situ measurements, *J. Geophys. Res.*, *112*, D09213, doi:10.1029/2006JD007202.
- Waliser, D. E., et al. (2009), Cloud ice: A climate model challenge with signs and expectations of progress, *J. Geophys. Res.*, *114*, D00A21, doi:10.1029/2008JD010015.
- Wang, Z., and K. Sassen (2002), Cirrus cloud microphysical property retrieval using lidar and radar measurements. Part I: Algorithm description and comparison with in situ data, *J. Appl. Meteorol.*, *41*, 218–229, doi:10.1175/1520-0450(2002)041<0218:CCMPRU>2.0.CO;2.
- Winker, D. M., W. H. Hunt, and M. J. McGill (2007), Initial performance assessment of CALIOP, *Geophys. Res. Lett.*, *34*, L19803, doi:10.1029/2007GL030135.
- Winker, D. M., et al. (2010), The CALIPSO mission: A global 3D view of aerosols and clouds, *Bull. Am. Meteorol. Soc.*, *91*, 1211–1229, doi:10.1175/2010BAMS3009.1.

- Yang, P., B. A. Baum, A. J. Heymsfield, Y. X. Hu, H.-L. Huang, S.-C. Tsay, and S. Ackerman (2003), Single-scattering properties of droxtals, *J. Quant. Spectrosc. Radiat. Transf.*, *79-80*, 1159–1169, doi:10.1016/S0022-4073(02)00347-3.
- Yang, Q., Q. Fu, and Y. Hu (2010), Radiative impacts of clouds in the tropical tropopause layer, *J. Geophys. Res.*, *115*, D00H12, doi:10.1029/2009JD012393.
- Young, S. A., and M. A. Vaughan (2009), The retrieval of profiles of particulate extinction from Cloud-Aerosol Lidar Infrared Pathfinder Satellite Observations (CALIPSO) data: Algorithm description, *J. Atmos. Ocean. Technol.*, *26*, 1105–1119, doi:10.1175/2008JTECHA1221.1.
- Zhou, C., A. E. Dessler, M. D. Zelinka, P. Yang, and T. Wang (2014), Cirrus feedback on interannual climate fluctuations, *Geophys. Res. Lett.*, *41*, 9166–9173, doi:10.1002/2014GL062095.